

Modulating Electrical Performances of In_2O_3 Nanofiber Channel Thin Film Transistors via Sr Doping

Longfei Song, Linqi Luo, Xuan Li, Di Liu, Ning Han, Lei Liu, Yuanbin Qin, Johnny C. Ho,* and Fengyun Wang*

Although In_2O_3 nanofibers (NFs) are considered as one of the fundamental building blocks for future electronics, the further development of these NFs devices is still seriously hindered by the large leakage current, low on/off current ratio ($I_{\text{on}}/I_{\text{off}}$), and large negative threshold voltage (V_{TH}) due to the excess carriers existed in the NFs. A simple one-step electrospinning process is employed here to effectively control the carrier concentration of In_2O_3 NFs by selectively doping strontium (Sr) element to improve their electrical device performance. The optimal devices (3.6 mol% Sr doping concentration) can yield the high field-effect mobility ($\mu_{\text{fe}} \approx 3.67 \text{ cm}^2 \text{ V}^{-1} \text{ s}^{-1}$), superior $I_{\text{on}}/I_{\text{off}}$ ratio ($\approx 10^8$), and operation in the energy-efficient enhancement-mode. High- κ Al_2O_3 thin films can also be employed as the gate dielectric to give the gate voltage greatly reduced by 10 \times (from 40 to 4 V) and the μ_{fe} substantially increased by 4.8 \times (to $17.2 \text{ cm}^2 \text{ V}^{-1} \text{ s}^{-1}$). The electrospun E-mode Sr- In_2O_3 NF field-effect transistors (NFFETs) can as well be integrated into full swing of inverters with excellent performances, further elucidating the significant advance of this electrospinning technique toward practical applications for future low-cost, energy-efficient, large-scale, and high-performance electronics.

1. Introduction


In the past decades, due to the unique properties, such as the excellent mechanical flexibility, brilliant electron transport quality, exceptional optical properties and many others, 1D semiconductor nanostructures have been widely explored as fundamental building blocks for various technological applications.^[1–8] Among many 1D candidates, In_2O_3 has particularly attracted increasing attention^[9–14] and the devices built on electrospun In_2O_3 nanofibers (NFs) as their active channel

layers have also been demonstrated with impressive characteristics in next-generation electronics,^[9–11] biological/chemical sensors,^[15–17] and photoelectrical detectors,^[18,19] etc. Even though the In_2O_3 material may not be the best material choice for the future sustainability because of the scarcity of In, it still attracts a great deal of attention due to its excellent electrical properties.^[20–22] For instance, Kim et al. demonstrated a solution-processed metal-oxide thin film transistors (e.g., In_2O_3 , IZO, ZnO) via combustion process at a temperature as low as $\approx 200^\circ\text{C}$, which yielded a high mobility of $13 \text{ cm}^2 \text{ V}^{-1} \text{ s}^{-1}$.^[20] Meng et al. fabricated a electrospun fiber-to-film processed metal-oxide thin film transistors (i.e., In_2O_3 , IZO, IZrZO) with Al_2O_3 dielectrics, where these devices displayed an impressive on/off current ratio of 10^7 and a field effect mobility of $25 \text{ cm}^2 \text{ V}^{-1} \text{ s}^{-1}$.^[21] The physical properties of In_2O_3 NFs could also be enhanced via crosslinking welding process developed by

Cui et al.^[22] However, until now, most of the 1D In_2O_3 -based devices are generally operated in the n-type depletion-mode (D-mode), particularly featured with a negative threshold voltage (V_{TH}), a high off-state current, and a low ratio of on-state/off-state current ($I_{\text{on}}/I_{\text{off}}$).^[9,23] This inadequate device performance can be predominantly attributed to the excess carriers existed in the In_2O_3 NFs or nanowires (NWs), which are typically originated from the oxygen vacancies acting as the donor-like defects. Notably, the large negative V_{TH} means that there is a non-zero channel current yielded at a zero gate

L. F. Song, L. Q. Luo, X. Li, D. Liu, Prof. F. Y. Wang
College of Physics and State Key Laboratory of Bio-Fibers and Eco-Textiles
Qingdao University
Qingdao 266071, China
E-mail: fywang@qdu.edu.cn

Prof. N. Han
State Key Laboratory of Multiphase Complex Systems
Institute of Process Engineering
Chinese Academy of Sciences
Beijing 100190, China

 The ORCID identification number(s) for the author(s) of this article can be found under <https://doi.org/10.1002/aelm.201800707>.

DOI: 10.1002/aelm.201800707

Prof. L. Liu
School of Materials Science and Engineering
Shandong University of Science and Technology
Qingdao 266590, China

Dr. Y. B. Qin
Center for Advancing Materials Performance from the Nanoscale
State Key Laboratory for Mechanical Behavior of Materials
Xi'an Jiaotong University
Xi'an 710049, China

Prof. J. C. Ho
Department of Materials Science and Engineering
City University of Hong Kong
Hong Kong 999077, China
E-mail: johnnyho@cityu.edu.hk

bias, which would consume much more energy than their counterparts operating in the enhancement-mode (E-mode). In fact, E-mode devices are highly preferred for the low-energy consumption and simple circuit integration as there is not any need to apply a gate voltage to switch off the transistors.

In any case, for the practical utilizations in large-scale circuits, the modulation of carrier concentration in the In_2O_3 NFs as well as the fabrication of E-mode In_2O_3 NF devices via facile and simple methods are still challenging. There are several methods to effectively modulate the transistor operation mode, which mainly include tuning the surface/interface properties of device channels, controlling the carrier concentration by doping and others. For example, Hong et al. demonstrated an effective modulation of the device V_{TH} and the transistor operation mode via the adjustment of surface roughness and diameter of the ZnO NW channels.^[24] In specific, the devices based on smooth ZnO NWs with the large diameter exhibit the negative V_{TH} , while the devices utilizing the rough ZnO NWs with the small diameter exhibit the positive V_{TH} .^[24] However, this method employing the surface/interface modulation is difficult to precisely control the device threshold voltage, which cannot be practically applied in the large-scale circuit integration. For doping, although Zou et al. have successfully fabricated the E-mode devices by doping metal elements, such as Al, Mg, and Ga, into In_2O_3 NWs during the NW synthesis via chemical vapor deposition (CVD),^[9] these nanomaterial processing schemes are still far from being compatible with the industrial manufacturing platform due to the rather high fabricating cost, rigorous process control, low production throughput, and complicated subsequent device fabrication scheme. On the other hand, the doping method would fit well for the electrospinning process, in which the doping concentration can be easily and precisely controlled by adjusting the composition of the starting precursor solution. Importantly, the dopant atoms/ions can also be uniformly dispersed and distributed in the obtained NFs. As compared with other synthesis methods, including CVD,^[9,10] molecular beam epitaxy (MBE),^[25,26] and hydrothermal schemes,^[27,28] electrospinning possesses several unique advantages, such as low cost, high throughput, and ease of process control.^[23] Without utilizing any complicated process procedure, expensive equipment and catalyst material, electrospinning can yield continuous and uniform NFs with the controllable morphology and aspect ratio for large-area applications.^[29,30]

At the same time, in our previous work, the D-mode devices based on In_2O_3 NF networks could be successfully transformed into E-mode operation by Mg doping during the one-step electrospinning process, while the corresponding electrical properties can be simply controlled by varying the amount of Mg dopant in the precursor solution.^[31] Even though these E-mode Mg- In_2O_3 NF field-effect transistors (NFFETs) have been demonstrated with the potential for high-performance, low energy consumption, and large-scale electronic devices, the required Mg doping concentration range is surprisingly very narrow, inducing great difficulties for the practical NF manufacturing process there. In this case, developing the doping process with alternative dopant elements is urgently needed. As compared with other possible dopant atoms, Sr has served as a promising dopant choice for other metal-oxide

thin film material systems.^[32] It is also well accepted that the large metal-oxide bond dissociation energy of constituents would negatively affect the charge transport properties of nanostructures. It is anticipated that the Sr-doped In_2O_3 NFs would exhibit the superior electrical properties as compared with the ones of Mg, La, and Sc atoms doped In_2O_3 NFs, since the bond dissociation energy of Sr-O (426 KJ mol⁻¹) is slightly higher than that of In-O (346 KJ mol⁻¹) but relatively smaller than those of Mg-O (561 KJ mol⁻¹), La-O (798 KJ mol⁻¹), and Sc-O (671 KJ mol⁻¹).^[33,34] Moreover, Sr dopants have also been utilized to enhance the stability of fabricated thin-film devices.^[33,35] For example, Avis and Jang demonstrated that Sr can not only reduce the negative bias illumination shift (NBIS) of ZnSnO thin film transistors, but also enhance the stability of devices.^[35] Besides, Parthiban and Kwon also confirmed that Sr-doped semiconductors would exhibit the enhanced device stability and reduced the V_{TH} shift.^[33] All these findings can evidently indicate that Sr elements can be an attractive dopant candidate among plenty of other metals, enhancing the electrical performance and stability of metal-oxide based electronic devices.

In this work, high-performance E-mode FETs based on electrospun Sr-doped In_2O_3 NF networks were successfully fabricated by a simple and one-step electrospinning technique. In specific, the NF/substrate adhesion could be effectively enhanced by using an UV-assisted pretreatment, which led to the further improvement in the device characteristics. For the optimal Sr doping concentration of 3.6 mol%, the obtained devices would exhibit the impressive electrical performance, including a high μ_{fe} of 3.67 cm² V⁻¹ s⁻¹ and a suitable V_{TH} of 4.8 V, a low off current of down to 10⁻¹¹ A, a high saturation current of up to 10⁻³ A, and a superior $I_{\text{on}}/I_{\text{off}}$ ratio of 10⁸. Furthermore, when the solution-processed Al_2O_3 high- κ dielectric was employed for the devices, the corresponding operation voltage could be substantially reduced from 40 V to below 4 V while the μ_{fe} could be boosted up to 17.2 cm² V⁻¹ s⁻¹. In addition, the resistor-loaded inverters based on optimized Sr- In_2O_3 NF network devices were also demonstrated, which yielded a full swing of excellent inverter characteristics with a large gain of 12.8. These circuit characteristics can clearly illuminate the significant advance of our Sr-doped In_2O_3 NFs toward the practical application for future low-cost, low-energy consumption and large-scale electronics.

2. Results and Discussions

Figure 1a shows the typical scanning electron microscope (SEM) image of In_2O_3 NF network fabricated by electrospinning, which indicates the high uniformity of obtained NF networks. Specifically, the as-synthesized In_2O_3 NFs have the relatively large diameters of 500–600 nm mainly composed of polyvinylpyrrolidone (PVP), residual solvent, and metal salts. Since the NFs are fabricated directly onto the dielectrics, the problem of “nanomaterial transfer,” being always existed in other nanomaterial manufacturing techniques such as CVD of NWs, can be completely eliminated. However, due to the overlapping of NFs, the initial NF networks would suffer from the poor interfacial adhesion between the NF device channel layer

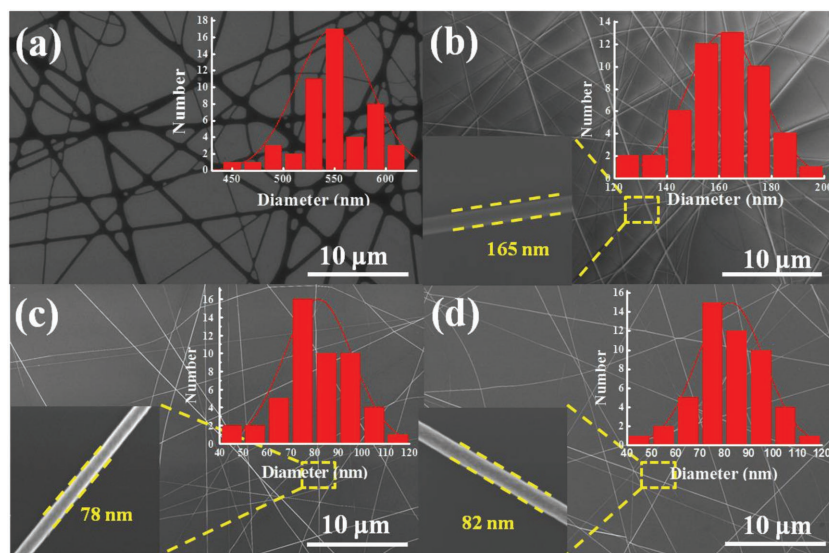


Figure 1. SEM images of 3.6 mol% Sr-In₂O₃ NFs at different experiment conditions with electrospinning time of 50 s: a) untreated by UV-assisted irradiation; b) treated by 40 min UV-assisted irradiation; c) 2 h thermal treatment at 600 °C after UV pretreatment; d) after the introduction of Sr dopants. Bottom insets show the corresponding zoom-in SEM images of single NF, respectively. Top insets give the corresponding statistics of the diameter based on 50 individual NFs in each sample group.

and the dielectric material, where these interfacial adhesion properties are known to play a key role for the subsequent carrier transport and fabricated device performances.^[15] In order to solve this problem and further enhance the device characteristics, a UV-assisted irradiation pretreatment is performed on the as-synthesized In₂O₃ NF networks. As shown in the SEM image of UV-treated In₂O₃ NF networks in Figure 1b, the NFs yield the reduced diameter of 150–200 nm, which suggests that the low molecular photoproducts (pyrrolidone and others) have been released due to the efficient UV absorption of PVP. The Figure 1b inset gives a zoomed-in image of a typical NF with a diameter of 165 nm and a uniform surface morphology. In order to enhance the NF crystallinity, the NFs are annealed at 600 °C for 2 h. After that, the high-quality NFs are obtained with further reduced diameters of 50–100 nm, indicating the removal of PVP (Figure 1c). In order to fully evaluate the NF diameters under different experimental conditions, diameter distributions of at least 50 individual NFs for each experimental condition were compiled as shown in the insets of Figure 1. At the same time, the Sr dopants can be introduced into the NFs during the spinning process and it is obvious that the Sr doping would not induce any associated change in the NF diameter and surface morphology (Figure 1d). More importantly, the NF network density (0.45–1.1 NF µm⁻¹) and the Sr doping concentration (3.6–18 mol%) can be effectively controlled by varying the electrospun time (30–60 s) and starting precursor concentration (Figure S1, Supporting Information). All these findings have confirmed the fabrication of uniform and dense NF networks with the smooth surface, which is essential for the succeeding device construction.

Next, detailed X-ray diffraction (XRD) studies are conducted to evaluate the incorporation of Sr dopants into the crystal lattice of In₂O₃. As depicted in Figure 2 in the Supporting Information,

there are several peaks at 21.45°, 30.54°, 35.43°, 45.63°, 50.96°, and 60.62°, which correspond to the (211), (222), (400), (431), (440), and (622) planes of the pure cubic In₂O₃, respectively (JCPDS 71-2194). For the 3.6 and 9 mol% Sr-doped NF samples, the XRD peak patterns are similar with that of pure cubic NFs, which suggests that there are not any other impurity phases, such as Sr, SrO_x, or InSrO_x, that existed except for the slight shift of the main (222) peak toward the left. This shift can be explained by using the Bragg's Law of $\lambda = 2d \sin \theta$, where λ is the fixed diffraction wavelength, d is interplanar crystal spacing, and θ is the diffraction angle. When Sr dopants are incorporated into the crystal structure of In₂O₃ NFs, the d value would increase due to the larger ionic radius of Sr (0.118 nm) as compared with that of In (0.08 nm), resulting in the decrease of θ and left shift of the XRD peak. It should also be noted that the XRD spectrum of the 18 mol% Sr-In₂O₃ NF sample is relatively complicated. There are peaks located at 22.38°, 32.63°, 45.65°, 57.21°, and 58.27° for the (012), (110), (024), (214), and (300) planes, accordingly,

of the rhombohedral In₂O₃ phase (JCPDS 72-0801). Except for the rhombohedral phase, the sample also exhibits a main peak of (222), which belongs to the cubic In₂O₃ phase and the peak of (141) belonging to the Sr₂In₂O₅ metal alloy phase (JCPDS 73-0629). These results indicate that when the Sr doping concentration is increased to 18 mol%, the mixed crystal phases occur^[36,37] and these mixed crystal phases can introduce lots of grain boundaries, which deteriorate the electronic transport properties of NFs.

In order to further investigate the crystal structure of both pure and Sr-doped In₂O₃ NFs, thorough electron microscopy is performed in addition to the XRD study. As shown in transmission electron microscope (TEM) image in Figure 2a, the annealed 3.6 mol% Sr-In₂O₃ NFs are straight with smooth surface and uniform diameter along their entire length, which are critical for electronic devices because any tapering or surface coating would seriously degrade the electrical transport properties of 1D nanomaterials.^[6] Based on the corresponding high-resolution transmission electron microscope (HRTEM) image (Figure 2b) and electron diffraction pattern (Figure 2c), the NF has the polycrystalline structure with relatively uniform crystalline grains. The interplanar spacing is measured to be 2.94 Å for the (222) plane, which is slightly larger than the ideal spacing of cubic In₂O₃ (≈2.92 Å), suggesting the incorporation of Sr dopants there. This result is also consistent with the XRD measurement, further confirming the formation of high-quality Sr-In₂O₃ NFs after calculation at 600 °C. Figure S3 in the Supporting Information also gives the TEM images of undoped, 3.6, 9, and 18 mol% Sr-doped In₂O₃ NFs. Again, there are not any noticeable change of the diameter and surface morphology of NFs that agree well with the SEM results discussed above. Notably, the interplanar spacings of the (222) plane of the pure, 3.6 and 9 mol% Sr-doped In₂O₃

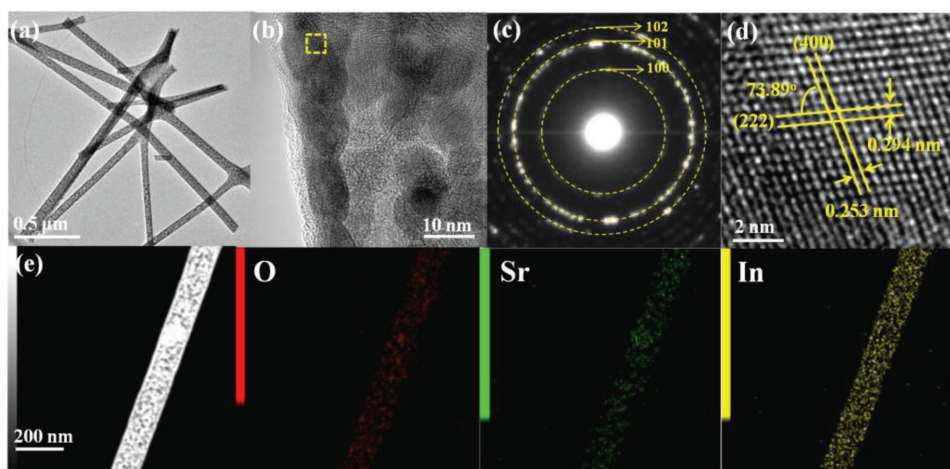


Figure 2. a) The bright field TEM image of 3.6 mol% Sr-In₂O₃ NFs. b) TEM image of 3.6 mol% Sr-In₂O₃ NF and c) the corresponding selected area electron diffraction (SAED). d) The HRTEM image of yellow box in image (b). e) The corresponding EDS elemental mapping.

NFs are measured to be 2.92, 2.96, and 3.1 Å, respectively. According to XRD, there are mixed crystal phases, containing both cubic and rhombohedral structures, for the 18 mol% Sr-In₂O₃ NF sample, which are confirmed by the HRTEM image. As illustrated in Figure S3d in the Supporting Information, the interplanar spacing of 2.76 Å corresponds to the (110) planes of rhombohedral In₂O₃ (JCPDS 72-1809), again being slightly larger than the ideal (110) planes (≈ 2.74 Å). These slight increases in the spacings are anticipated due to the incorporation of Sr elements into the In₂O₃ crystal lattice as the diameter of Sr dopants is larger than that of In atoms. Moreover, element energy dispersive X-ray spectroscopy (EDS) mapping is as well carefully carried out on all fabricated NFs (Figure 2e). It can be revealed that distribution of In, Sr, and O constituents are very uniform along both axial and radial direction of the NF.

Simultaneously, it is important to assess the bandgap changes of In₂O₃ NFs when the Sr doping concentration varies. In this case, the optical absorption spectra of all fabricated NFs, which can indicate a Burstein–Moss shift, are measured as shown in Figure 3. The bandgap of NFs

can be determined from the maximum curvature of the $(Ah\nu)^{1/2}-(h\nu)$ curves (Figure 3 inset). They are founded to be 3.17, 3.23, 3.31, and 3.3 eV for pure, 3.6, 9, and 18 mol% Sr-doped In₂O₃ NFs, respectively. With an aim to fully identify the bandgap changes of In₂O₃ NFs after Sr doping, the average and standard deviation of the corresponding band gaps were measured based on six samples, which were 3.15 ± 0.03 , 3.25 ± 0.04 , 3.32 ± 0.03 , and 3.29 ± 0.02 eV for pure, 3.6, 9, and 18 mol% Sr-doped In₂O₃ NFs, respectively. These bandgaps increase distinctively with the increasing Sr doping concentration except for the 18 mol% doped sample of Sr-In₂O₃ NFs. As Sr atoms have a standard electrode potential of -4.1 V, they can easily react with oxygen as compared with the In atoms, having a standard electrode potential of -0.34 V. This way, when Sr atoms are doped into the In₂O₃ lattice, the concentration of oxygen vacancies would be decreased and resulted to the reduction of density of state in the band structure, leading to the bandgap reduction.^[38] As a result, the bandgap of In₂O₃ NFs would increase with the amount of Sr dopants incorporated there. It should be noted that the bandgap of 18 mol% Sr-In₂O₃ NFs is slightly smaller than

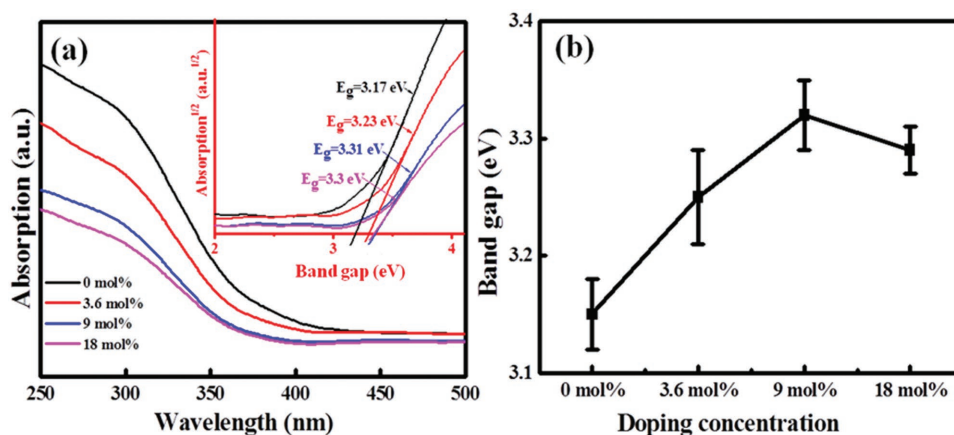


Figure 3. a) Absorption spectra for undoped, 3.6, 9, and 18 mol% Sr-doped NFs, respectively, and the inset is the corresponding $(Ah\nu)^{1/2}-(h\nu)$ curves. b) Statistical data of the band gap measured for different Sr concentrations of Sr-In₂O₃ NFs.

that of 9 mol% Sr-In₂O₃ NFs, which can be attributed to the phase conversion of In₂O₃ from cubic ($E_g = 3.75$ eV) to rhombohedral ($E_g = 3.02$ eV). With the enlargement of these bandgaps, the electrons in NFs would need more excitation energy when they jump from the valence band into the conduction band, leading to the reduced off-state device current and enhanced I_{on}/I_{off} ratio, etc., being advantageous for practical applications.

To shed light on the electrical properties of all NF networks-based devices, FETs are fabricated in the common back-gated configuration using Al as source/drain metal contacts, thermally grown 150 nm thick SiO₂ as the gate dielectric and heavily doped p-type Si substrate as the back-gate. **Figure 4a** exhibits the SEM image of one typical In₂O₃ NFFET together with its schematic illustration. Specifically, the density of In₂O₃ NF networks is controlled to be 0.6 NFs μm^{-1} with the electrospun time of ≈ 30 s, which give the best device performance in the current investigation. Either too low or too high density of NFs would lead to the poor device performance, while the V_{TH} value is observed to be insensitive to the NF density here. For example, when the NF density is too low, it cannot supply enough carriers to obtain high saturation current. Although high density of NFs can produce the high saturation current because of its higher carrier concentration, it can give rise to the relatively high off-state current and low I_{on}/I_{off} ratio. It needs to be emphasized that all the devices are fabricated under the same experimental conditions and characterized with the same voltage sweeping rate in order to ensure a consistent comparison among all the device characterizations. As shown in the typical transfer characteristics in **Figure 4b**, all devices exhibit the n-type conducting behaviors. Although the pure In₂O₃ NFFET gives a relative large saturation current of 7.5×10^{-4} A and a high μ_{fe} of $4.8 \text{ cm}^2 \text{ V}^{-1} \text{ s}^{-1}$, it also has a

high off-state current of 2.4×10^{-6} A, and a large negative V_{TH} of -14.2 V (**Figure 4e**). It is worth noting that the V_{TH} value is obtained from the horizontal intercept of linear regimes in $I_{DS}^{1/2}$ versus V_{GS} curve. The μ_{fe} is measured by using the following formula, which is widely accepted to calculate μ_{fe} for conventional thin film transistors:

$$I_{DS} = [(W/2L)C_i\mu_{fe}](V_{GS} - V_{TH})^2 \quad (1)$$

where W and L are the channel width and length of device, and C_i is areal capacitance of dielectrics.^[31] These high off-state current, low I_{on}/I_{off} ratio, and large V_{TH} values are mainly attributed to the excessive carrier concentration originated from the oxygen vacancies in the NFs, where these vacancies act as the electron donor for metal-oxide materials. Because the electronegativity of Sr element (0.95) is smaller than that of In (1.7), Sr possesses stronger metallicity and facilitate the formation of Sr–O bonds more easily as compared with that of In–O bonds, which can then be applied as an “oxygen getter” in order to reduce the oxygen vacancies to suppress excess carriers in the In₂O₃ NFs.^[39]

With the purpose of modulating device performance and optimizing doping concentration, the devices based on Sr-In₂O₃ NF networks with various doping concentrations are fabricated and systematically investigated. When the 2 mol% Sr-doped In₂O₃ NFs are fabricated into devices, even though their device off-state current get reduced to 4.0×10^{-8} A, the I_{on}/I_{off} ratio is still only 10^4 with the V_{TH} value of -6.9 V for the D-mode device operation. When the Sr doping concentration is further increased to 3.6 mol%, the off-state current is as low as 7.9×10^{-11} A with the impressively high I_{on}/I_{off} ratio of 10^8 . More importantly, the corresponding V_{TH} is obviously right shifted to 2.5 V, indicating successful conversion from D-mode into E-mode for the device operation. Moreover, the device still

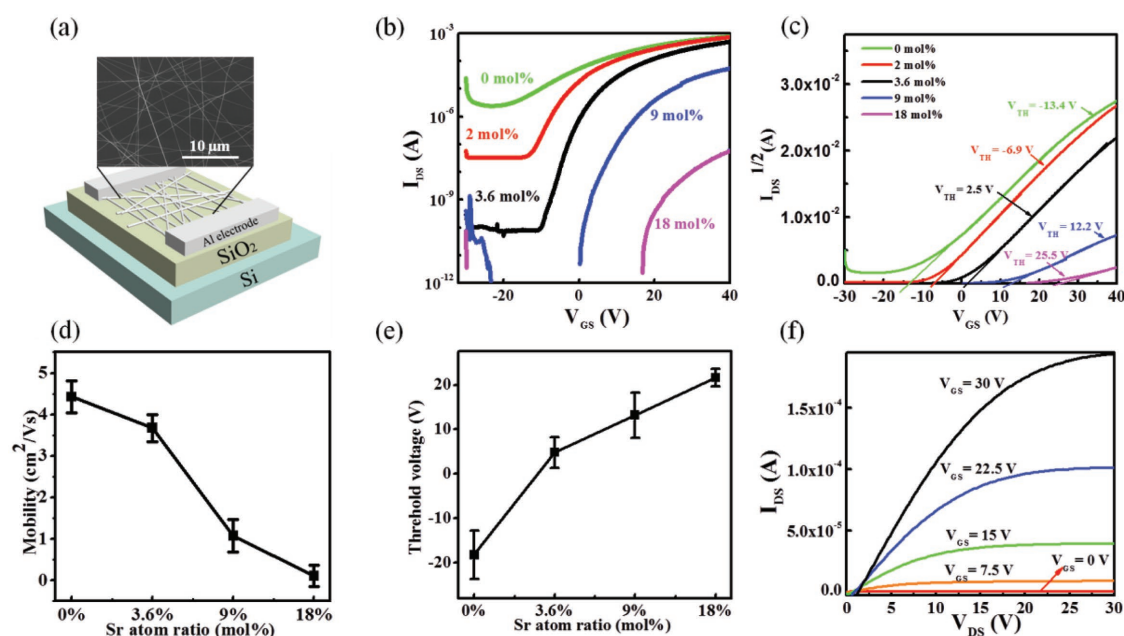


Figure 4. a) Schematic diagram of NFFET, inset is the SEM image of In₂O₃ NFs. b) Transfer characteristic of undoped, 2, 3.6, 9, and 18 mol% Sr-In₂O₃ devices, respectively. c) V_{TH} corresponding to the transfer curves in (b). d) The corresponding average field effect mobility. e) The corresponding average V_{TH} of all Sr-In₂O₃ devices. f) Output characteristic of 3.6 mol% Sr-In₂O₃/SiO₂ device.

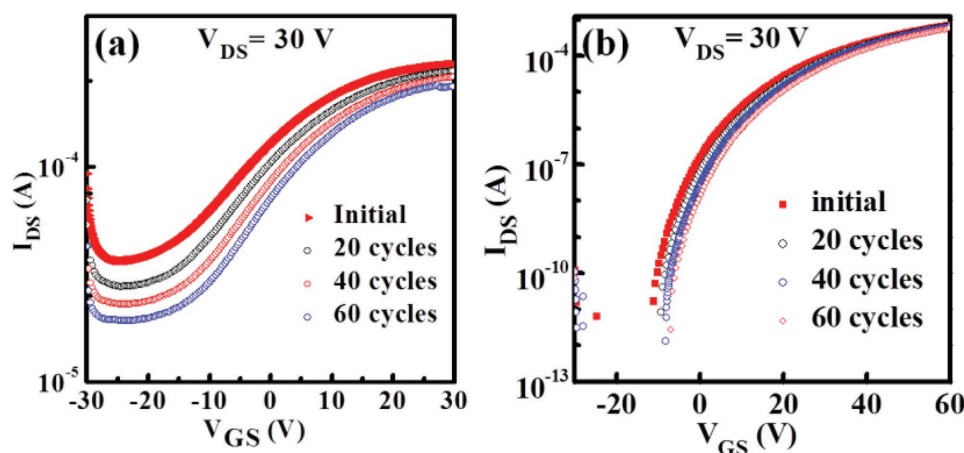


Figure 5. a) Transfer curves of $\text{In}_2\text{O}_3/\text{SiO}_2$ NF device after multiple cycle measurements. b) Transfer curves of 3.6 mol% $\text{Sr-In}_2\text{O}_3/\text{SiO}_2$ NF device after multiple cycle measurements.

shows a decent mobility of $3.92 \text{ cm}^2 \text{ V}^{-1} \text{ s}^{-1}$ which is only a slight drop as compared with 2 mol% $\text{Sr-In}_2\text{O}_3$ NFFETs. When the doping concentration is enlarged to 9 and 18 mol%, the off-state current can be further decreased down to 4.7×10^{-12} and $2.4 \times 10^{-12} \text{ A}$, respectively; however, the saturation current would also get reduced to 5.3×10^{-5} and $5.7 \times 10^{-8} \text{ A}$, accordingly, seriously limiting their use for electronics. In this case, the optimal Sr doping concentration is found to be 3.6 mol%. As compared with the optimal Mg doping concentration of 2 mol% in the previous work,^[31] the saturation current of 3.6 mol% $\text{Sr-In}_2\text{O}_3$ NFFETs increases by 4.4× and the mobility increases by 1.8×, which indicate that the device electrical performance can be effectively enhanced by controlling the Sr doping concentration.

To further understand the relationships between the device performance and the doping concentration, a statistical analysis of 20 devices for every doping concentration is performed. As shown in Figure 4d, the μ_{fe} value is decreased drastically from 4.43 to $0.11 \text{ cm}^2 \text{ V}^{-1} \text{ s}^{-1}$ with the increasing Sr doping concentration from 0 to 18 mol%. The decreasing tendency of the mobility is attributed to these positive scattering centers or scattering interfaces induced by Sr atoms, which can change the direction of electron motion and reduce their velocity, leading to the remarkable suppression of the electron mobility. Furthermore, for the increasing Sr doping concentration, the device V_{TH} can be positively shifted to 21.62 V (Figure 4e), indicating that the Sr dopants can effectively transfer the NF device operation from D-mode into E-mode and reduce the energy consumption for device operation. The detailed device performance data are summarized in Table S1 in the Supporting Information. Figure 4f shows the typical output characteristics of the 3.6 mol% $\text{Sr-In}_2\text{O}_3$ NFFET, which exhibits distinct pinch-off and linear-saturation region. The other corresponding output characteristics of pure In_2O_3 , 9 and 18 mol% $\text{Sr-In}_2\text{O}_3$ NFs are also shown in Figure S4 in the Supporting Information, respectively. All these would illustrate that the devices with optimal Sr doping concentration of 3.6 mol% exhibit a promising potential for the high-performance electronic devices.

In general, the operation stability is another important device performance parameter. In this case, the transfer

characteristics of pure and 3.6 mol% Sr-doped In_2O_3 NF devices are carefully compared after different cycles of operation. As depicted in Figure 5a, after 60 cycles, the V_{TH} of the pure In_2O_3 NF networks device exhibit an obviously positive-shift of 5.5 V, which can be mainly ascribed to existence of defect sites, such as surface states or crystal defects. Besides, the saturation current of the device after 60 cycles decreases 1.7× as compared with the initial cycle. On the other hand, as shown in Figure 5b, the V_{TH} of the 3.6 mol% $\text{Sr-In}_2\text{O}_3$ NF networks device only displays a positive-shift of 2.4 V, indicating the enhanced stability of Sr-doped NFs as device channels. The saturation current also shows a very stable value as compared with the initial cycle. All these results indicate that Sr dopants can reduce the amount of defect sites and enhance the device stability, which can be due to its higher Gibbs energy of oxidation as compared with In and other dielectric element (e.g., Mg, Hf, Si, Y). Typically, the defect sites (N_t) can be calculated by the following formula:

$$N_t = \left[\frac{SS \cdot \log(e)}{\frac{KT}{q}} - 1 \right] \frac{C_{\text{ox}}}{q}$$

where SS is the subthreshold slope, K is the Boltzmann constant, T is temperature, e is the base of natural logarithm, C_{ox} is the capacitance per unit area of the gate insulator, and q is the electron charge, respectively.^[40] In specific, SS can be obtained from the transfer characteristics, in which it is defined as dV_g/dI_d . Based on Figure 5a,b, the SS value of the pure In_2O_3 NFFET is obviously smaller than that of the 3.6 mol% $\text{Sr-In}_2\text{O}_3$ device. N_t was measured to be 5.5×10^{12} and $0.29 \times 10^{12} \text{ cm}^{-2}$ for pure In_2O_3 NFFET and 3.6 mol% $\text{Sr-In}_2\text{O}_3$, individually. The lower N_t was not only beneficial to the charge carrier transport, but also the device operation stability. All these findings can fully illustrate that the optimal Sr doping can effectively reduce the defect concentration and enhance the device stability.

With the aim to further minimize the operation voltage and improve the device performance, solution-processed Al_2O_3 thin film is also utilized as the high- κ dielectrics. As compared with

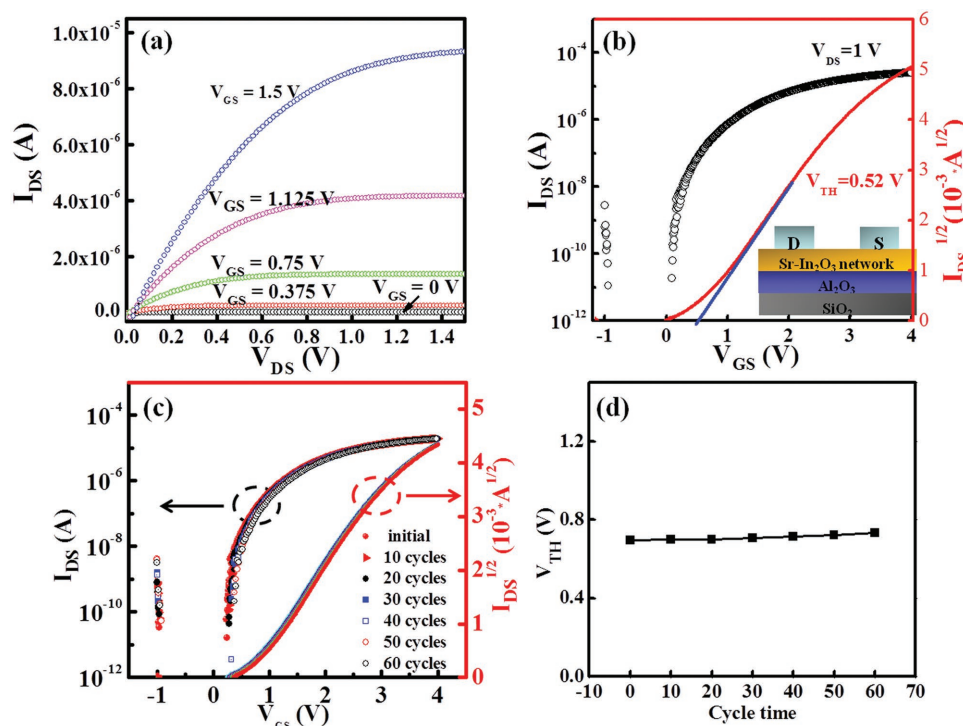


Figure 6. a) Output characteristic of 3.6 mol% Sr-In₂O₃/Al₂O₃ device. b) Transfer characteristic of 3.6 mol% Sr-In₂O₃/Al₂O₃ device (black line) and the corresponding $I_{DS}^{1/2}$ – V_{GS} curves (red line). Inset is the corresponding device schematic. c) Transfer curves at different stress times (black axis) and corresponding $I_{DS}^{1/2}$ versus V_{GS} curves (red axis). d) The corresponding V_{TH} value corresponding to different cycle times.

conventional SiO₂ dielectrics, Al₂O₃ film has been widely used as gate-insulating layer for thin film transistors due to its high dielectric constant (8–10), large bandgap (8.7 eV), low interface trap density with compound semiconductors, large conduction band offset with silicon substrate ($\Delta E < 3$ eV), high breakdown electric field (4–5 MV cm^{−1}), low oxygen diffusion coefficient, and outstanding thermal stability. **Figure 6a** gives the output characteristics of the 3.6 mol% Sr-doped In₂O₃ device with Al₂O₃ dielectrics, which exhibits a clear linear-saturation region with the ohmic-like contact property. **Figure 6b** shows the corresponding transfer characteristics (black line). The device exhibits a large I_{on}/I_{off} ratio of 10⁶, which is determined by the high saturation current of 10^{−5} A and the low off-state current of 10^{−11} A. Moreover, the enhanced μ_{fe} is obtained to be as high as 17.2 cm² V^{−1} s^{−1}. Besides, 20 as-fabricated device channels fabricated on the same wafer were measured with the statistics presented in **Figure S5** in the Supporting Information, which exhibit the devices with small electrical performance deviation of μ_{fe} (16.0–18.0 cm² V^{−1} s^{−1}) and V_{TH} (0.3–0.9 V). Importantly, the operation voltage is currently 4 V, reduced by 10× as compared with that of the 3.6 mol% Sr-In₂O₃ doped device with the same device structure and dimension, which is important for the low-power consumption electronic devices. In order to further verify and ensure the device stability, the device transfer characteristics are repeatedly measured with different cycles (**Figure 6c**). It is clear that the electrical parameters, such as the on-state current, off-state current, and I_{on}/I_{off} ratio, yield the negligible change after 60 cycles. The V_{TH} shift is only 0.05 V after 60 cycles of measurements (**Figure 6d**), highlighting the superior device stability of our Sr-doped In₂O₃ NF networks devices.

It is also noted that the device hysteresis is typically dependent on the crystal defects and/or surface states of the channel materials, while this hysteresis is also one of the key parameters for the device performance evaluation. In this work, the device hysteresis based on 3.6 mol% Sr-In₂O₃ NFs with SiO₂ and Al₂O₃ film as gate insulators was assessed and depicted in **Figure S6** in the Supporting Information. It exhibits a relatively small hysteresis of 2.6 V for 3.6 mol% Sr-In₂O₃/SiO₂ NFFETs and 0.03 V for 3.6 mol% Sr-In₂O₃/Al₂O₃ NFFETs, respectively. In addition, the aging effect of Sr-In₂O₃ NFFETs was also investigated after storing the device in controlled environment (25 °C in temperature, 30% in humidity) for 8 months as displayed in **Figure S7** in the Supporting Information. The devices yield an excellent stability with a relatively small V_{TH} shift of 2.05 and 0.05 V for 3.6 mol% Sr-In₂O₃/SiO₂ NFFET and Sr-In₂O₃/Al₂O₃ NFFET, respectively, as well as a negligible decrease of the on-current of 9.8×10^{-5} and 1.0×10^{-7} A, accordingly. All these findings further confirm the stability of the devices for practical deployment.

At the end, it is also critical to investigate the compatibility of NF devices for circuit integration. Among many circuit components, inverters are widely considered as the fundamental element which can be fabricated based on E-mode devices. In this work, the resistance-loaded inverter is constructed with an E-mode 3.6 mol% Sr-doped In₂O₃ NF networks device and a resistor of 10 MΩ. As demonstrated in the typical voltage transfer characteristics of the fabricated inverter in **Figure 7a**, it is obvious that a full swing of inverter characteristic is resulted with the input and output signals effectively rectified. The corresponding voltage gain (defined as $-dV_{out}/dV_{in}$) is found to be 3.4 in maximum at a V_{DD} of 25 V (**Figure 7b**). When the Al₂O₃ high- κ dielectric is employed, the

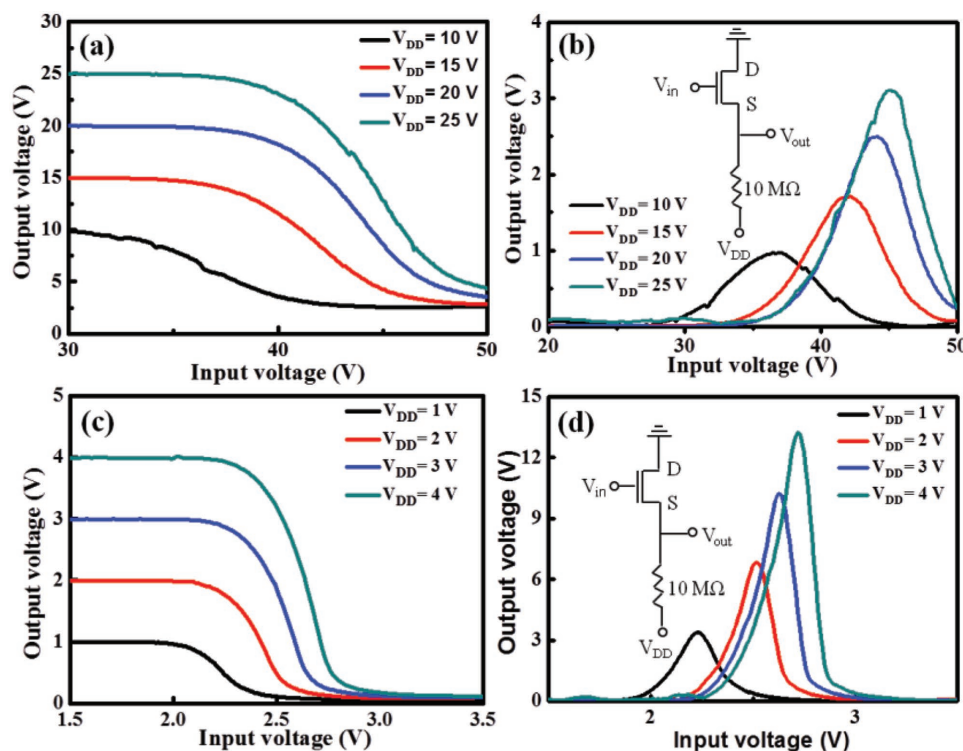


Figure 7. a) Voltage transfer characteristic and b) the corresponding gains of the resistor-loaded inverter based on electrospun 3.6 mol% Sr-In₂O₃/SiO₂ devices. Inset in (b) is circuit schematic of the resistor-loaded inverter. c) Voltage transfer characteristic and d) corresponding gains of the resistor-loaded inverter based on electrospun 3.6 mol% Sr-In₂O₃/Al₂O₃ devices. Inset in (d) is circuit schematic of the resistor-loaded inverter.

inverter characteristics can be substantially enhanced with a maximum voltage gain of 12.8 (Figure 7c,d). All these results illustrate that the fabricated devices exhibit promising potential in the practical applications of large-scale logic circuits.

3. Conclusion

In conclusion, the high-performance enhancement-mode transistors based on Sr-doped In₂O₃ NFs networks are successfully fabricated via a simple one-step electrospinning process. Importantly, the electrical properties of In₂O₃ NF devices can be precisely modulated by controlling the Sr doping concentration. For the optimal Sr doping concentration of 3.6 mol%, the devices can exhibit a high μ_{fe} (3.67 cm² V⁻¹ s⁻¹), a suitable threshold voltage (0–5 V), a low I_{off} (10⁻¹¹ to 10⁻¹⁰ A), a high I_{on} (10⁻⁴ to 10⁻³ A), and a superior I_{on}/I_{off} ratio (10⁷ to 10⁸). Moreover, when the Al₂O₃ dielectric is utilized, the corresponding operation voltage can be reduced by 10×, which exhibits the promising potential for low-cost, low energy consumption, and high-performance devices. Moreover, the device operating stability has been further investigated and confirmed with the measurement of difference cycles. To further demonstrate the versatility of our Sr-doped NFs, resistor-loaded inverters based on optimal Sr-doped In₂O₃ NFs devices are fabricated and characterized, where the invertors yield the efficient response with a decent voltage gain. All of these results have clearly presented a significant advance toward the practical application of electrospun NFFETs for future low-cost, low energy consumption, large-scale, and high-performance electronics.

4. Experimental Section

Solution-Processed Precursor Preparation and NF Electrospinning Process: The In₂O₃ precursor solution was prepared by dissolving 0.2 g of indium chloride tetrahydrate (InCl₃·4H₂O, 99.9%, Aladdin) and 0.8 g of PVP (MW of 1 300 000 g mol⁻¹, Aladdin) into 5 mL of N,N-Dimethylformamide (DMF). Various amounts of strontium nitrate (Sr(NO₃)₂, 99.8%, Aladdin), ranging from 2.0 to 18.0 mol% corresponded to the mole ratio of Sr (mole (Sr)/mole (Sr)+mole (In)) existed in the precursor, was applied as the source of Sr and was completely dissolved in DMF. Then, the obtained solution was stirred at room temperature for 12 h.

For dielectrics, the Al₂O₃ precursor solution was prepared by dissolving 0.1 M of aluminum nitrate (Al(NO₃)₃·9H₂O) in 10 mL of DMF. Subsequently, the solution was stirred at room temperature for more than 12 h in order to enhance the solution homogeneity. Before processing, the precursor solution was filtered by using the 0.22 μm polytetrafluoroethylene (PTFE) syringe filter.

NFFET Fabrication: The clear precursor solution was delivered to a syringe with a stainless-steel needle, which had an inner diameter of 0.5 mm. The horizontal distance between the stainless-steel needle and the static collector (aluminum foil) was maintained at 12 cm with an applied DC voltage of 15 kV and a flow rate of 0.5 mL h⁻¹ using a syringe pump (2.5 mL). Then, the thermally grown 100 nm thick SiO₂/Si (p+) wafer (1.5 cm × 1.5 cm) was adhered to the aluminum foil while the ejected NFs was also collected onto the SiO₂/Si substrate. The optimal electrospun time is 30 s. The processed samples were next baked at 150 °C for 10 min, followed by the UV-assisted irradiation for 40 min. After that, the samples were annealed at 600 °C for 2 h and the heating rate was 10 °C min⁻¹. Finally, Al source and drain electrodes were evaporated thermally through a shadow mask with the finished device channel dimension of 1000 μm in width and 100 μm in length.

To integrate the FETs with high-κ dielectrics, the thermally grown SiO₂ dielectrics was replaced by the solution-processed Al₂O₃ thin film. A

p-type heavily doped Si wafer with the clean surface was first treated with oxygen plasma for 5 min to enhance its surface hydrophilicity. Then, the Al_2O_3 precursor solution was spin-coated onto the processed Si wafer at a fixed speed of 5000 rpm for 12 s. Subsequently, the wafer was placed on a hot plate and baked at 150 °C for 10 min. The baked film was then illuminated under the UV light for 40 min. The UV lamp power was 1 kW and the wavelength range was between 200 and 400 nm. Finally, the baked thin film was annealed at 700 °C for 3 h in the air. Notably, all experiment processes were conducted under the same conditions (i.e., 25 °C in temperature and 30% in humidity).

NF and FET Characterization: The NF morphology and crystal structure were characterized by SEM (NovaNano SEM450, operated at 15 keV), TEM (JEOL JEM 2100F, operated at 200 kV), HRTEM (JEOL JEM 2100F, operated at 200 kV), selected area electron diffraction (SAED, JEOL JEM 2100F, operated at 200 kV), and XRD (Rigaku D/max-rB). The elemental distribution of obtained Sr-doped In_2O_3 NFs was analyzed by the EDS (Oxford Instrument and EDAX Inc, attached to the HRTEM). The absorption spectrum was measured by a UV-vis spectrophotometer (PERSEE, T9). The electrical properties of prepared NFFETs were measured in ambient conditions by using a semiconductor parameter analyzer (Keithley 2634B) and a probe station.

Supporting Information

Supporting Information is available from the Wiley Online Library or from the author.

Acknowledgements

The work was financially supported by the Natural Science Foundation of Shandong Province, China (ZR2018JL021, ZR2014EMQ011), the National Natural Science Foundation of China (51402160), the National Key R&D Program of China (2016YFC0207100), and the Taishan Scholar Program of Shandong Province, China. The work was also supported by the State Key Laboratory of Multiphase Complex Systems (MPCS-2015-A-04), Opening Project of Key Laboratory of Microelectronic Devices and Integrated Technology, Institute of Microelectronics, Chinese Academy of Sciences, the Key Laboratory of Advanced Energy Materials Chemistry (Ministry of Education), Nankai University, Tianjin 300071, China and the General Research Fund of the Research Grants Council of Hong Kong SAR, China (CityU 11211317).

Conflict of Interest

The authors declare no conflict of interest.

Keywords

enhancement mode, high performance, In_2O_3 nanofiber, inverter, Sr element

Received: October 9, 2018

Revised: December 8, 2018

Published online: January 13, 2019

- [1] H. Anzai, M. Suzuki, K. Nagashima, M. Kanai, Z. Zhu, Y. He, M. Boudot, G. Zhang, T. Takahashi, K. Kanemoto, T. Seki, N. Shibata, T. Yanagida, *Nano Lett.* **2017**, *17*, 4698.
- [2] M. S. Yao, W. X. Tang, G. E. Wang, B. Nath, G. Xu, *Adv. Mater.* **2016**, *28*, 5229.
- [3] H. Zhu, Y. Fu, F. Meng, X. Wu, Z. Gong, Q. Ding, M. V. Gustafsson, M. T. Trinh, S. Jin, X.-Y. Zhu, *Nat. Mater.* **2015**, *14*, 636.

- [4] N. Han, F. Y. Wang, J. J. Hou, S. P. Yip, H. Lin, F. Xiu, M. Fang, Z. X. Yang, X. Shi, G. Dong, T. F. Hung, J. C. Ho, *Adv. Mater.* **2013**, *25*, 4445.
- [5] H. Ko, Z. Zhang, J. C. Ho, K. Takei, R. Kapadia, Y. L. Chueh, W. Cao, B. A. Cruden, *Small* **2010**, *6*, 22.
- [6] N. Han, F. Wang, A. T. Hui, J. J. Hou, G. C. Shan, X. Fei, T. F. Hung, J. C. Ho, *Nanotechnology* **2011**, *22*, 285607.
- [7] A. C. Ford, S. Chuang, J. C. Ho, Y. L. Chueh, A. Javey, *Nano Lett.* **2010**, *10*, 509.
- [8] Y. Li, F. Qian, J. Xiang, C. M. Lieber, *Mater. Today* **2006**, *9*, 18.
- [9] X. Zou, X. Liu, C. Wang, Y. Jiang, Y. Wang, X. Xiao, J. C. Ho, J. Li, C. Jiang, Q. Xiong, L. Liao, *ACS Nano* **2012**, *7*, 804.
- [10] Z. Zhou, C. Lan, S. P. Yip, R. Wei, D. Li, L. Shu, J. C. Ho, *Nano Res.* **2018**, *11*, 5935.
- [11] C. Lee, P. Srisungsitthisunti, S. Park, S. Kim, X. Xu, K. Roy, D. B. Janes, C. Zhou, S. Ju, M. Qi, *ACS Nano* **2011**, *5*, 1095.
- [12] P. Nguyen, H. T. Ng, T. Yamada, M. K. Smith, J. Li, J. Han, M. Meyyappan, *Nano Lett.* **2004**, *4*, 651.
- [13] C. Li, J. Ly, B. Lei, W. Fan, D. Zhang, J. Han, M. Meyyappan, M. Thompson, C. Zhou, *J. Phys. Chem. B* **2004**, *108*, 9646.
- [14] C. Li, W. Fan, D. A. Straus, B. Lei, S. Asano, D. Zhang, J. Han, M. Meyyappan, C. Zhou, *J. Am. Chem. Soc.* **2004**, *126*, 7750.
- [15] D. Zhang, Z. Liu, C. Li, T. Tang, X. Liu, S. Han, B. Lei, C. Zhou, *Nano Lett.* **2004**, *4*, 1919.
- [16] L. Liu, S. Li, X. Guo, L. Wang, L. Liu, X. Wang, *J. Mater. Sci.: Mater. Electron.* **2016**, *27*, 5153.
- [17] S. H. Wang, S. J. Chang, S. Liu, T. Y. Tsai, C. L. Hsu, *IEEE Sens. J.* **2016**, *16*, 5850.
- [18] X. Liu, L. Gu, Q. Zhang, J. Wu, Y. Long, Z. Fan, *Nat. Commun.* **2014**, *5*, 4007.
- [19] S. Chen, Y. Z. Long, H. D. Zhang, S. L. Liu, L. Z. Liu, J. C. Zhang, G. X. Liu, F. K. Shan, *Phys. Scr.* **2014**, *89*, 115808.
- [20] M. G. Kim, M. G. Kanatzidis, A. Facchetti, T. J. Marks, *Nat. Mater.* **2011**, *10*, 382.
- [21] Y. Meng, A. Liu, Z. Guo, G. Liu, B. Shin, Y. Y. Noh, E. Fortunato, R. Martins, F. Shan, *ACS Appl. Mater. Interfaces* **2018**, *10*, 18057.
- [22] Y. Cui, Y. Meng, Z. Wang, C. Wang, G. Liu, R. Martins, E. Fortunato, F. Shan, *Nanoscale* **2018**, *10*, 19427.
- [23] Y. Meng, G. Liu, A. Liu, Z. Guo, W. Sun, F. Shan, *ACS Appl. Mater. Interfaces* **2017**, *9*, 10805.
- [24] W. K. Hong, J. I. Sohn, D. K. Hwang, S. S. Kwon, G. Jo, S. Song, S. M. Kim, H. J. Ko, S. J. Park, M. E. Welland, T. Lee, *Nano Lett.* **2008**, *8*, 950.
- [25] K. H. Zhang, A. Walsh, C. R. A. Catlow, V. K. Lazarov, R. G. Egdell, *Nano Lett.* **2010**, *10*, 3740.
- [26] M. C. Jeong, B. Y. Oh, M. H. Ham, S. W. Lee, J. M. Myoung, *Small* **2007**, *3*, 568.
- [27] J. Yang, C. Lin, Z. Wang, J. Lin, *Inorg. Chem.* **2006**, *45*, 8973.
- [28] G. Shen, P. C. Chen, K. Ryu, C. Zhou, *J. Mater. Chem.* **2009**, *19*, 828.
- [29] Y. Dai, W. Liu, E. Formo, Y. Sun, Y. Xia, *Polym. Adv. Technol.* **2011**, *22*, 326.
- [30] S. Huang, G. Ou, J. Cheng, H. Li, W. Pan, *J. Mater. Chem. C* **2013**, *1*, 6463.
- [31] H. Zhang, Y. Meng, L. Song, L. Luo, Y. Qin, N. Han, Z. Yang, L. Liu, J. C. Ho, F. Wang, *Nano Res.* **2017**, *3*, 1227.
- [32] J. H. Park, Y. B. Yoo, K. H. Lee, W. S. Jang, J. Y. Oh, S. S. Chae, W. J. Choi, H. K. Baik, *Appl. Phys. Express* **2012**, *5*, 111101.
- [33] S. Parthiban, J. Y. Kwon, *J. Mater. Res.* **2014**, *29*, 1585.
- [34] Y. R. Luo, *Comprehensive Handbook of Chemical Bond Energies*, CRC Press, Boca Raton, FL **2007**.
- [35] C. Avis, J. Jang, *ECS Trans.* **2014**, *64*, 101.
- [36] M. M. Fan, K. W. Liu, X. Chen, X. Wang, Z. Z. Zhang, B. H. Li, D. Z. Shen, *ACS Appl. Mater. Interfaces* **2015**, *7*, 20600.

- [37] O. Lupan, V. Cretu, V. Postica, N. Ababii, O. Polonskyi, V. Kaidas, F. Schütt, Y. K. Mishra, E. Monaico, I. Tiginyanu, V. Sontea, T. Strunskus, F. Faupel, R. Adelung, *Sens. Actuators, B* **2016**, 224, 434.
- [38] J. Singh, P. Kumar, K. S. Hui, K. Hui, K. Ramam, R. Tiwari, O. Srivastava, *CrystEngComm* **2012**, 14, 5898.
- [39] J. W. Hennek, J. Smith, A. Yan, M.-G. Kim, W. Zhao, V. P. Dravid, A. Facchetti, T. J. Marks, *J. Am. Chem. Soc.* **2013**, 135, 10729.
- [40] A. Liu, G. X. Liu, H. H. Zhu, H. J. Song, B. Shin, E. Fortunato, R. Martins, F. K. Shan, *Adv. Funct. Mater.* **2015**, 25, 7180.